2012-08

Binding of molecular magnesium hydrides to a zirconocene-enyne template

Angewandte Chemie International Edition,Weinheim : Wiley-VCH Verlag,v. 51, n. 35, p. 8846-8849, Aug. 2012
http://www.producao.usp.br/handle/BDPI/49502

Solid State Sciences 14 (2012) 367–374

Contents lists available at SciVerse ScienceDirect

Solid State Sciences

journal homepage: www.elsevier.com/locate/ssscie

^{7}Li and ^{29}Si solid state NMR and chemical bonding of $La_2Li_2Si_3$

Thorsten Langer [a], Sven Dupke [b], Hellmut Eckert [b], Samir F. Matar [c], Martin Winter [b], Rainer Pöttgen [a,*]

[a] Institut für Anorganische und Analytische Chemie, Westfälische Wilhelms-Universität Münster, Corrensstrasse 30, D-48149 Münster, Germany
[b] Institut für Physikalische Chemie, Universität Münster, Corrensstrasse 30,D-48149 Münster, Germany
[c] CNRS, Université de Bordeaux, ICMCB, 87 Avenue du Docteur Albert Schweitzer, 33600 Pessac, France

ARTICLE INFO

Article history:
Received 10 October 2011
Received in revised form
22 December 2011
Accepted 29 December 2011
Available online 6 January 2012

Keywords:
Lithium
Crystal chemistry
Solid state NMR
Chemical bonding

ABSTRACT

The ternary silicide $La_2Li_2Si_3$ was synthesized from the elements in a sealed niobium tube. $La_2Li_2Si_3$ was characterized by powder and single crystal X-ray diffraction: $Ce_2Li_2Ge_3$ type, *Cmcm*, $a = 450.03(8)$, $b = 1880.3(4)$, $c = 689.6(1)$ pm, $wR2 = 0.0178$, 597 F^2 values, and 26 parameters. The $La_2Li_2Si_3$ structure contains two crystallographically independent silicon sites, both in slightly distorted trigonal prismatic coordination. The Si1 atoms are located in condensed La_6 prisms and form cis–trans chains (two-bonded silicon) with Si1–Si1 distances at 238 and 239 pm, indicating single bond character. The Si2 atoms are isolated within La_2Li_4 prisms. $La_2Li_2Si_3$ might be formally considered as an electron precise Zintl phase with an electron partition $(2La^{3+})(2Li^{+})(2Si1^{2-})(Si2^{4-})$. Electronic structure calculations show a trend in this direction based on a charge density analysis with large electron localization around the Si1–Si1 chains. The compound is found weakly metallic with chemical bonding reminiscent of LaSi and additional features brought in by Li and Si2. High resolution solid state ^{7}Li and ^{29}Si MAS-NMR spectra are in agreement with the crystal structural information, however, the ^{29}Si resonance shifts observed suggest strong Knight shift contributions, at variance with the Zintl concept. Variable temperature solid state ^{7}Li spectra indicate the absence of motional narrowing on the kHz timescale within the temperature range $300K < T < 400$ K.

1. Introduction

Nano- and bulk-silicon have intensively been studied in recent years with respect to lithiation for use as alternative electrode materials in lithium ion batteries [1–3, and refers. therein]. Silicon anodes have much higher specific capacity and capacity density than carbon. The mechanisms of silicon lithiation and delithiation are still not completely understood. Key problems are crystalline-to-amorphous phase transitions of the Li_xSi phases. A highly useful tool for examination of the Li_xSi phases is solid state NMR spectroscopy on the ^{6}Li, ^{7}Li, and ^{29}Si nuclei. Two different strategies have been pursued. One possibility is the in-situ or ex-situ characterization of the phases formed during the charge/discharge cycles [4,5] and on the other hand detailed NMR spectroscopic characterization [6–8] of binary lithium silicides [9] is indispensable as a basic characterization.

In continuation of our synthetic/solid state NMR approach on the binary lithium silicides [6–8] we started to investigate ternary silicides $Li_xT_ySi_z$ (T = transition metal) [10] and $Li_xRE_ySi_z$ (RE = rare earth metal) [11] with respect to crystal chemistry, chemical bonding, and lithium mobility. The rare earth metal based systems Li–*RE*–Si have so far only scarcely been investigated. So far only $CeLi_{0.34}Si_{1.66}$, CeLiSi [12], and $Gd_{0.75}Li_{0.75}Si_{1.5}$ [13] with $ThSi_2$ structure, $CeLiSi_2$ with the $LiCaSi_2$ type [12], Eu_2LiSi_3 [14], YLiSi [15], LiY_2Si_2 and $LiNd_2Si_2$ [16], as well as the series $RE_2Li_2Si_3$ (*RE* = La, Ce, Pr, Nd, Sm) [12,17,18] have been characterized. All these studies focussed on the synthesis and structure determination and in the case of the $RE_2Li_2Si_3$ series some magnetic data [18] have been reported. A remarkable result is the surprisingly high Curie temperature of 17 K for $Ce_2Li_2Si_3$.

Herein we report on the structure, a combined ^{7}Li and ^{29}Si solid state NMR characterization, and a study of chemical bonding of the lanthanum compound $La_2Li_2Si_3$.

2. Experimental

2.1. Synthesis

Starting materials for the synthesis of $La_2Li_2Si_3$ were lithium rods (Merck, > 99.5%), lanthanum ingots (Johnson Matthey, > 99.9%)

* Corresponding author. Tel.: +49 251 83 36001; fax: +49 251 83 36002.
E-mail addresses: eckerth@uni-muenster.de (H. Eckert), matar@icmcb-bordeaux.cnrs.fr (S.F. Matar), pottgen@uni-muenster.de (R. Pöttgen).

1293-2558/$ – see front matter © 2012 Elsevier Masson SAS. All rights reserved.
doi:10.1016/j.solidstatesciences.2011.12.012

and silicon pieces (Wacker, > 99.9%). The lithium rods were cut into smaller pieces under dry paraffin oil and subsequently washed with *n*-hexane. The lithium pieces were kept in Schlenk tubes under argon prior to the reaction. An appropriate piece of the lanthanum ingot was cut and arc-melted [19] to a small button under an argon atmosphere. Argon was purified with titanium sponge (900 K), silica gel, and molecular sieves. The lithium pieces were mixed with the lanthanum button and the silicon pieces in an atomic ratio of 4:2:3 under flowing argon and then arc-welded in a niobium ampoule under an argon pressure of about 700 mbar. The niobium tube was then placed in the water-cooled sample chamber of an induction furnace [20] (Hüttinger Elektronik, Freiburg, Germany, Typ TIG 2.5/300). The sample was rapidly heated to 1450 K and held at that temperature for 15 min. Subsequently, the sample was cooled to 1000 K within 10 min and kept at that temperature for another 48 h before the reaction was quenched by switching off the power supply. The sample could readily be separated from the tube and no reaction with the container material was observed. The excess of lithium was removed with ethanol (> 99%). Single crystals exhibit metallic lustre whereas ground powders are dark grey.

2.2. EDX data

The $La_2Li_2Si_3$ single crystal studied on the diffractometer was analyzed using a Zeiss EVO MA10 scanning electron microscope. LaB_6 and SiO_2 were used as standards for the semiquantitative EDX analysis. No impurity elements heavier than sodium were observed. The experimentally determined composition La : Si of 38 ± 2:62 ± 2 was close to the ideal one (40:60).

2.3. X-ray diffraction

The polycrystalline $La_2Li_2Si_3$ sample was characterized by powder X-ray diffraction on a Guinier camera (equipped with an image plate system Fujifilm, BAS-1800) using Cu Kα_1 radiation and α-quartz ($a = 491.30$, $c = 540.46$ pm) as an internal standard. The orthorhombic lattice parameters (Table 1) were deduced from a least-squares fit of the powder data. Correct indexing of the diffraction lines was ensured by an intensity calculation [21] using the positional parameters obtained from the structure refinement. Our lattice parameters agree well with the data given recently by Merlo et al. of $a = 450.4(1)$, $b = 1882.9(3)$, $c = 689.7(1)$ pm [18].

Well shaped crystal fragments of $La_2Li_2Si_3$ were obtained by mechanical fragmentation from the regulus prepared by high-frequency annealing. The crystals were glued to quartz fibres using a two component adhesive. Their quality for intensity data collection was checked by Laue photographs on a Buerger camera (white molybdenum radiation, image plate technique, Fujifilm, BAS-1800). A suitable crystal was measured at room temperature on an IPDS II diffractometer (graphite monochromatized Mo Kα radiation; oscillation mode). A numerical absorption correction was applied to the data set. All relevant crystallographic data and details of the data collection and evaluation are listed in Table 1.

Table 1
Crystallographic data and structure refinement for $La_2Li_2Si_3$.

Empirical formula	$La_2Li_2Si_3$
Molar mass (g mol^{-1})	375.97
Space group; *Z*	*Cmcm*; 4
Structure type	$Ce_2Li_2Ge_3$
Lattice parameters (pm)	$a = 450.03(8)$
(Guinier powder data)	$b = 1880.3(4)$
	$c = 689.6(1)$
Cell volume (nm^3)	$V = 0.5835(2)$
Crystal size (μm^3)	40 × 40 × 120
Calculated density (g cm^{-3})	4.28
Transm. ratio (max/min)	0.745/0.443
Radiation	Mo K_α
λ, pm	71.073
Absorption coefficient (mm^{-1})	14.9
F(000), *e*	648
θ range (°)	2–32
Range in *hkl*	±6, ±27, ±10
Total reflections	3619
Independent reflections/R_{int}	597/0.0238
Reflections with $I \geq 2\sigma(I)/R_\sigma$	556/0.0133
Data/parameters	597/26
Goodness-of-fit	1.018
$R1/wR2$ for $I \geq 2\sigma(I)$	0.0093/0.0165
$R1/wR2$ for all data	0.0122/0.0178
Extinction coefficient	0.0096(1)
Largest diff. peak/hole (e Å^{-3})	0.74/−0.60

2.4. Structure refinement

Careful analysis of the $La_2Li_2Si_3$ data set showed a *C*-centred orthorhombic lattice and the systematic extinctions were compatible with space group *Cmcm*. Since isotypy of the lanthanum compound with $Ce_2Li_2Ge_3$ [17] and $Nd_2Li_2Si_3$ [18] was already evident from the Guinier powder pattern, the atomic parameters of $Nd_2Li_2Si_3$ [18] were taken as starting values and the structure was refined with anisotropic displacement parameters for all atoms with SHELXL-97 (full-matrix least-squares on F_o^2) [22,23]. The very good data quality even allowed anisotropic refinement of the lithium site. Refinement of the occupancy parameters of the lanthanum and silicon sites gave no hint for deviations from the ideal composition. The refinement went smoothly to the residuals listed in Table 1. The final difference electron density synthesis was flat. The positional parameters and interatomic distances are listed in Tables 2 and 3. Further details on the structure refinement may be obtained from the Fachinformationszentrum Karlsruhe, D-76344 Eggenstein-Leopoldshafen (Germany), by quoting the Registry No. CSD–423611.

2.5. Electronic structure calculations methodology

The most appropriate theoretical framework for electronic structure and energy related quantities is density functional theory (DFT) [24,25] within which we use two complementary computational methods. The Vienna *ab initio* simulation package (VASP) code [26,27] allows geometry optimization and subsequent establishment of the energy–volume equation of states (EOS). For this we use the projector augmented wave (PAW) method [28] (particularly accurate for studying rare earths), built within the generalized gradient approximation (GGA) scheme following Perdew, Burke and Ernzerhof (PBE) [29]. The conjugate-gradient algorithm [30] is used in this computational scheme to relax the atoms of the different structural setups. The tetrahedron method with Blöchl corrections [28] as well as a Methfessel-Paxton [31] scheme was applied for both geometry relaxation and total energy calculations. Brillouin zone (BZ) integrals were approximated using the special k-point sampling of Monkhorst and Pack [32]. The optimization of the structural parameters was performed until the forces on the atoms were less than 0.02 eV/Å and all stress components less than 0.003 eV/Å^3. The calculations are converged at an energy cut-off of 250 eV for the plane-wave basis set with respect to the k-point integration with a starting mesh of 4 × 4 × 4 up to 8 × 8 × 8 for best convergence and relaxation to zero strains.

Then all-electron calculations, equally based on the DFT with GGA-PBE functional [29], are carried out for a full description of the electronic structure and the properties of chemical bonding. They are performed using the full potential scalar-relativistic augmented spherical wave (ASW) method [33,34]. In the ASW method, the

Table 2
Atomic coordinates and anisotropic displacement parameters (pm^2) for $La_2Li_2Si_3$. U_{eq} is defined as one third of the trace of the orthogonalized U_{ij} tensor. $U_{12} = U_{13} = 0$.

Atom	Wyckoff site	*x*	*y*	*z*	U_{11}	U_{22}	U_{33}	U_{23}	U_{eq}
La1	4*c*	0	0.44796(1) *0.448*[a]	1/4	61(1)	62(1)	54(1)	0	59(1)
La2	4*c*	0	0.65979(1) *0.659*	1/4	65(1)	62(1)	98(1)	0	75(1)
Li	8*f*	0	0.18701(15) *0.188*	0.5619(4) *0.561*	78(14)	76(13)	56(13)	−32(10)	70(6)
Si1	8*f*	0	0.05673(2) *0.057*	0.07664(1) *0.077*	91(2)	66(2)	64(2)	−3(2)	74(1)
Si2	4*c*	0	0.28038(4) *0.280*	1/4	74(3)	78(3)	137(3)	0	97(1)

[a] Values given in italics derive from a geometry optimization with the lattice parameters $a = 450.5$, $b = 1880.2$, $c = 690.8$ pm, and $V = 0.5848$ nm^3.

wave function is expanded in atom-centred augmented spherical waves, which are Hankel functions and numerical solutions of Schrödinger's equation, respectively, outside and inside the so-called augmentation spheres. In the minimal ASW basis set, we choose the outermost shells to represent the valence states and the matrix elements were constructed using partial waves up to $l_{max} + 1 = 4$ for La, *i.e.*, 4*f* states were considered within the basis set, $l_{max} + 1 = 3$ for Si and $l_{max} + 1 = 2$ for Li. Self-consistency was achieved when charge transfers and energy changes between two successive cycles were such as: $\Delta Q < 10^{-8}$ and $\Delta E < 10^{-6}$ eV, respectively. The Brillouin zone integrations were performed using the linear tetrahedron method within the irreducible wedge [28]. The calculations are carried out assuming spin degenerate configuration. Besides the site projected density of states, we discuss qualitatively the pair interactions based on the overlap population analysis with the crystal orbital overlap population (COOP) [35]. In the plots, positive, negative, and zero COOP magnitudes indicate bonding, anti-bonding, and non-bonding interactions, respectively. Here we use the integrated *i*COOP criterion to address relative bonding intensities. We note that another scheme for describing the chemical bonding, the ECOV (covalent bond energy) criterion based on both the overlap and the Hamiltonian populations is also accessible within the ASW method [33,34]. It provides similar qualitative results to the COOP.

2.6. Solid state NMR

All the NMR experiments were conducted on a Bruker DSX 400 spectrometer. Variable temperature static ^{7}Li NMR spectra were obtained using a commercial static 5 mm Bruker probe tuned at 155.55 MHz. Spectra were acquired using a $90_x^\circ - t - 90_y^\circ$ solid echo sequence using a 90° pulse length of 4 μs and a relaxation delay of 20 s, ^{7}Li and ^{29}Si MAS-NMR spectra were acquired using a commercial 4 mm MAS Bruker probe tuned at 155.55 and 79.58 MHz, respectively. 90° pulses of 4 and 5.25 μs length and relaxation delays of 20 and 30 s, respectively, were used for measuring the ^{7}Li and the ^{29}Si MAS-NMR spectra. Rotor frequencies of 10 and 15 kHz were used. To avoid probe detuning effects by these metallic samples, the material was mixed with dried boron nitride in a 1:1 mass ratio. Lineshape simulations were conducted using the DMFIT software [36].

Table 3
Interatomic distances (pm) in the structure of $La_2Li_2Si_3$, calculated with the powder lattice parameters. Standard deviations are less or equal 0.3 pm.

La1	1	Si2	315.1	Li	1	Li	259.5
	4	Si1	318.5		1	Si1	262.9
	4	Si1	326.7		2	Si2	266.9
	4	Li	363.1		1	Si2	277.6
	2	La1	396.5		2	La2	315.4
	1	La2	398.3		1	La2	315.9
	2	La2	399.9	Si1	1	Si1	238.1
La2	4	Li	315.4		1	Si1	239.1
	2	Li	315.9		1	Li	262.9
	2	Si2	319.4		2	La1	318.5
	4	Si1	320.1		2	La2	320.1
	2	Si2	362.7		2	La1	326.7
	1	La1	398.3	Si2	4	Li	266.9
	2	La1	399.9		2	Li	277.6
					1	La1	315.1
					2	La2	319.4
					2	La2	362.7

3. Results and discussion

3.1. Crystal chemistry

$La_2Li_2Si_3$ crystallizes with the orthorhombic $Ce_2Li_2Ge_3$ type structure [17], space group *Cmcm*. This structure type has so far been observed for the series $RE_2Li_2Si_3$ (RE = La, Ce, Pr, Nd) [18], $RE_2Li_2Ge_3$ (RE = La, Ce, Pr, Nd, Sm) [17], $Sr_2LiMgSi_3$ [37], $Eu_2Li_{1.16}Mg_{0.84}Ge_3$ and $Sr_2Li_{0.94}Mg_{1.06}Ge_3$ [38], $Eu_2LiMgSn_3$, and $Sr_2LiMgSn_3$ [39]. The present structure refinement of $La_2Li_2Si_3$ shows the highest precision among all $Ce_2Li_2Ge_3$ type compounds.

A projection of the $La_2Li_2Si_3$ structure along the short unit cell axis is presented in Fig. 1. The structure contains two crystallographically independent silicon sites, both in slightly distorted trigonal prismatic coordination. The *isolated* (no Si–Si bonding) Si2 atoms are located in Li_4La_2 prisms, while the Si1 atoms have La_6 prisms. The rectangular sites of both prism types are capped by further atoms, two Si1 plus one Li atom for Si1 and two Li plus one La1 atom for Si2. These tri-capped trigonal prisms, coordination number 9, are the typical silicon coordination found in diverse silicide structure types [40,41]. The $Si1La_6$ trigonal prisms are condensed via common rectangular faces, forming zigzag chains along the *c* direction, similar to the low-temperature structure of LaSi (Fig. 2) [42]. This condensation leads to silicon chains in *cis–trans* configuration with Si1–Si1 distances of 238 and 239 pm, close to elemental silicon (235 pm Si–Si) [43]. These chains certainly exhibit single bond character.

Besides Si1–Si1, the shortest interatomic distances in the $La_2Li_2Si_3$ structure occur for Li–Li (260 pm) and Li–Si (263–278 pm). The Li–Li distances are significantly shorter than in the cubic body-centred structure of elemental lithium (304 pm) [43]. Considering that all lithium atoms are almost fully ionized (see the NMR results below), these short distances are not surprising and they cannot be considered as signifying bonding interactions. Similar short Li–Li distances have been observed in $Li_3Pt_2Sn_3$ [44] and Li_4Pt_3Si [45]. The Li–Si distances range from 263 to 278 pm, slightly longer than the sum of the covalent radii of 240 pm [46]. Such Li–Si distances typically occur also in the binary silicides, e. g. $Li_{12}Si_7$ (259–309 pm) [47]. The Li–Si contacts in $La_2Li_2Si_3$ can only be considered as weakly bonding (*vide infra*). Together the lithium and silicon atoms build up a three-dimensional $[Li_2Si_3]$ network, in which the lanthanum atoms are located in larger cavities (Fig. 3).

To a first approximation the chemical bonding in $La_2Li_2Si_3$ can be discussed in the context of the Zintl concept. The two lanthanum and one lithium atoms per formula unit donate eight valence electrons which need to be distributed to the silicon atoms. Within

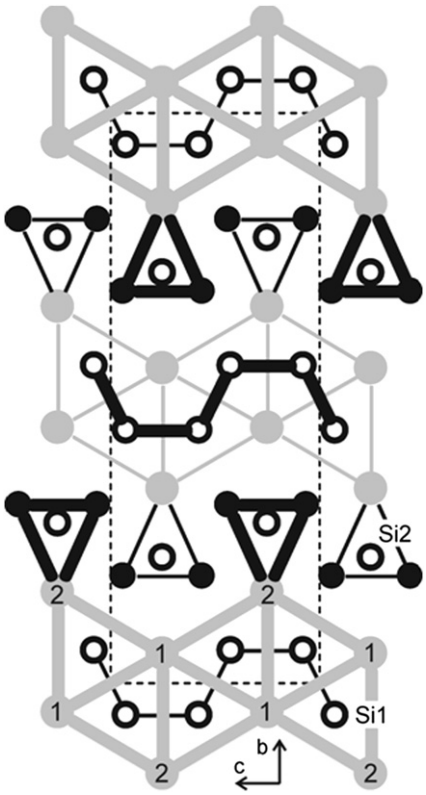

Fig. 1. Projection of the $La_2Li_2Si_3$ structure onto the *yz* plane. Lanthanum, lithium, and silicon atoms are drawn as medium grey, black filled, and open circles, respectively. All atoms lie on mirror planes at $x = 0$ (thin lines) and $x = 1/2$ (thick lines). The crystallographically independent lanthanum and silicon sites and the trigonal prismatic coordination of the silicon atoms are emphasized.

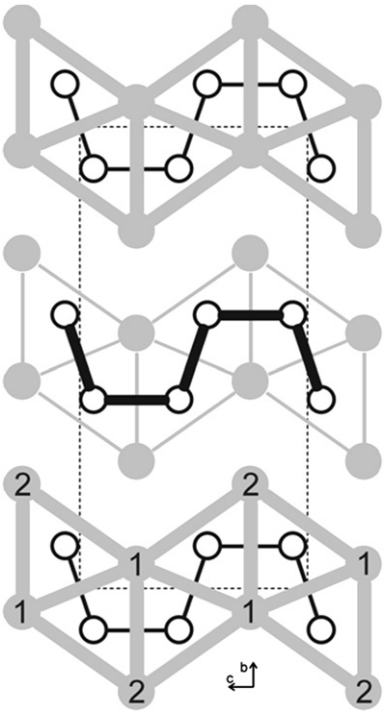

Fig. 2. Projection of the structure of the low-temperature modification of LaSi [42] onto the *yz* plane. Lanthanum and silicon atoms are drawn as medium grey and black open circles, respectively. All atoms lie on mirror planes at $x = 0$ (thin lines) and $x = 1/2$ (thick lines). The crystallographically independent lanthanum sites and the trigonal prismatic coordination of the silicon atoms are emphasized.

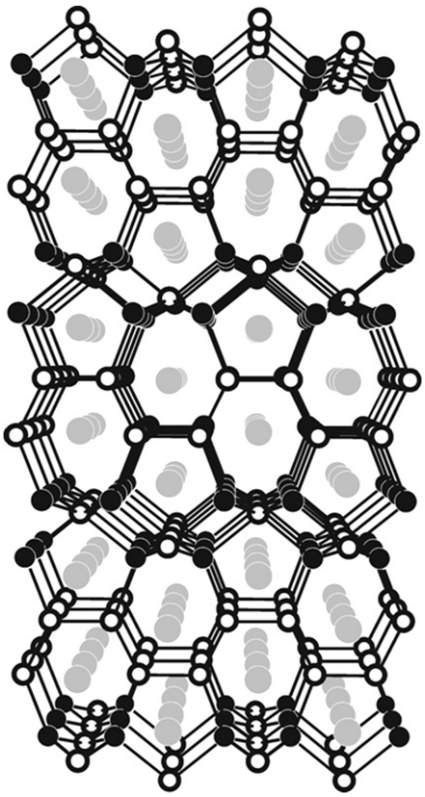

Fig. 3. Perspective view of the $La_2Li_2Si_3$ structure approximately along the *x*-axis. Lanthanum, lithium, and silicon atoms are drawn as medium grey, black filled, and open circles, respectively. The three-dimensional $[Li_2Si_3]$ network is emphasized.

the Zintl concept the *isolated* silicon atoms are considered as silicide anions Si^{4-} and the two-bonded Si1 atoms within the chain are counted as Si^{2-} Zintl anions, isoelectronic with sulphur. This model would lead to a description of $La_2Li_2Si_3$ as an electron precise Zintl phase $(2La^{3+})(2Li^{+})(2Si1^{2-})(Si2^{4-})$ –formally (*cf.* calculated charges), similar to the binary lithium silicides [9,48]. For a deeper understanding of chemical bonding in $La_2Li_2Si_3$ we performed electronic structure calculations which are addressed in the next chapter.

3.2. Results of geometry optimization and energy–volume equation of state

Geometry optimizations were carried out for $La_2Li_2Si_3$ starting from the X-ray diffraction results (Tables 1 and 2). Further, for the sake of establishing comparisons, similar studies were done on LT-LaSi [42] which presents similarities with the title compound: it crystallizes in the same *Cmcm* space group type and has La occupying two (4*c*) positions and Si (8*f*) like Si1 in $La_2Li_2Si_3$ (Figs. 1 and 2).

The optimization of the lattice parameters and the atomic positions provide good agreement with the experiment (*cf.* Table 2). Similarly good agreement was obtained for LaSi. With these optimized parameters we illustrate the electron distribution using the localization function ELF [49] obtained from real space calculations. It is normalized between 0 (zero localization, blue areas) and 1 (strong localization, red areas) with the value of 1/2 corresponding to a free electron gas behaviour. Fig. 4 shows the ELF contour plots for the zigzag like chains of Si shown in Figs. 1 and 2 for the title compound and for LaSi. From the red contours around the red (Si) spheres there is strong electron localization around

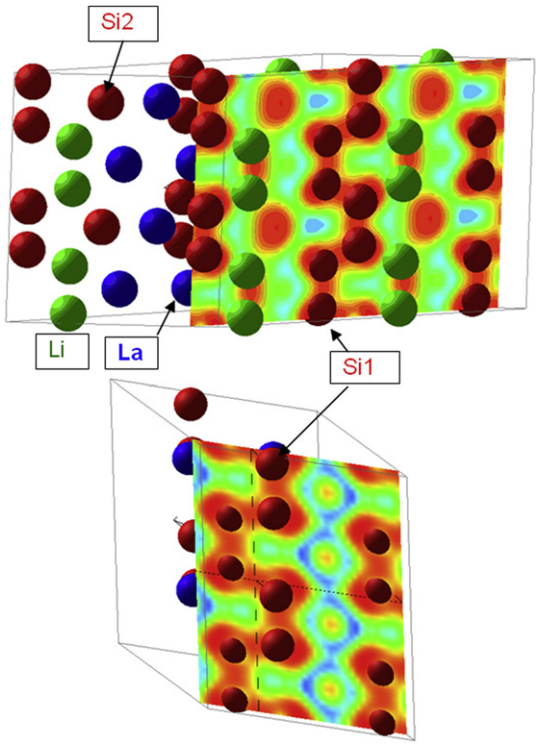

Fig. 4. Electron localization function (ELF) slice in $La_2Li_2Si_3$ (top) and LaSi (bottom) featuring Si–Si (red spheres) chains of Si (Si1 in $La_2Li_2Si_3$) with strong electron localization while green contours between them signal a nearly free electron gas behaviour in between chains (Li (green) and La (blue) spheres). (For interpretation of the references to colour in this figure legend, the reader is referred to the web version of this article.)

silicon, whereas there is a nearly free electron like behaviour (green) in between them. Then one expects charge transfer from La and Li towards the Si sites. In order to better assess this feature, we analyzed the charge density issued from the self consistent calculations using the Bader AIM (atoms in molecules theory) approach [50]. The changes of charge ΔQ results are as follows:

$La_2Li_2Si_3$ averaged values < La> +1.2, <Li> +1, <Si1> −1.1, <Si2> −2.2,

LaSi averaged values < La> +1.1 < Si> −1.1

pointing into the direction of the charge distribution predicted by the Zintl description (*vide infra*).

While the calculations yield the expected complete electron transfer from Li yielding Li^+, and positively/negatively ionized La/Si, the amounts of the charge transfers of the latter do not translate to fully ionized La and Si. Thus, for Si1 the charge is only −1.1 instead of −2 and for Si2 the charge is only −2.2 instead of −4. This is not unexpected in view of the Pauling electronegativities $\chi = 0.98$, 1.1, 1.9, resp. for Li, La and Si (Li being the most electropositive element) and indicates a quantum mixing between the valence states of La and Si in an overall covalent manner, i. e. opposite to ionic-like electron exchange. The larger negative charge for Si2 can be attributed to the absence of Si–Si bonding and the close Li–Si2 neighbourhood with 3 counter anions (Table 3).

3.3. Electronic structure and chemical bonding

In as far as the optimized lattice parameters are in good agreement with experiment, we use the latter (Table 1) to analyze the electronic structure and the chemical bonding using all electrons calculations with the full potential ASW method. The site projected density of states (PDOS) for both $La_2Li_2Si_3$ and LaSi are shown in Fig. 5. In both panels and in the following ones of the COOP, the zero energy along the *x*-axis is at the Fermi level (E_F). Also site multiplicities (*cf.* Table 2) are accounted for in all plots.

Comparing the two panels, the lanthanum (La1/La2) PDOS are dominating and they present similarities in their shapes and their centring and localization (sharp peaks) within the conduction band (CB) due to the empty *f* states. They are found closer to the Fermi level in the ternary silicide than in LaSi which is due to the additional electrons brought in by Li. The remaining itinerant (delocalized) PDOS which ensure for the chemical bond are crossing E_F and they extend within the valence band (VB) with low intensity but similar shapes, see the similar Si1(Si)/La1/La2 PDOS. Note however the localized and isolated less similar PDOS peaks at ∼ −7 eV and −1 eV, *s* and *p* like states for Si2 in the ternary silicide signalling a different behaviour in the quantum mixing with respect to Si1 whose *s* and *p* states extend on broader range (−10, −6 eV) and (−4, E_F), respectively. Li PDOS are of low intensity and they follow the shape of the other PDOS. The Fermi level crosses the DOS at very low intensity of itinerant states arising from all constituents in both compounds but with a larger intensity in LaSi which should be a better metal than $La_2Li_2Si_3$ which resembles more a semi-metal. This is in agreement with the formal Zintl conform charge distribution $La^{3+}Si^{2-}e^-$ as well as the temperature dependence of the electrical resistivity [42].

The chemical bonding features are illustrated in Fig. 6 in two panels for the title compound and for LaSi for the sake of comparison. Comparing the two panels, similar features are

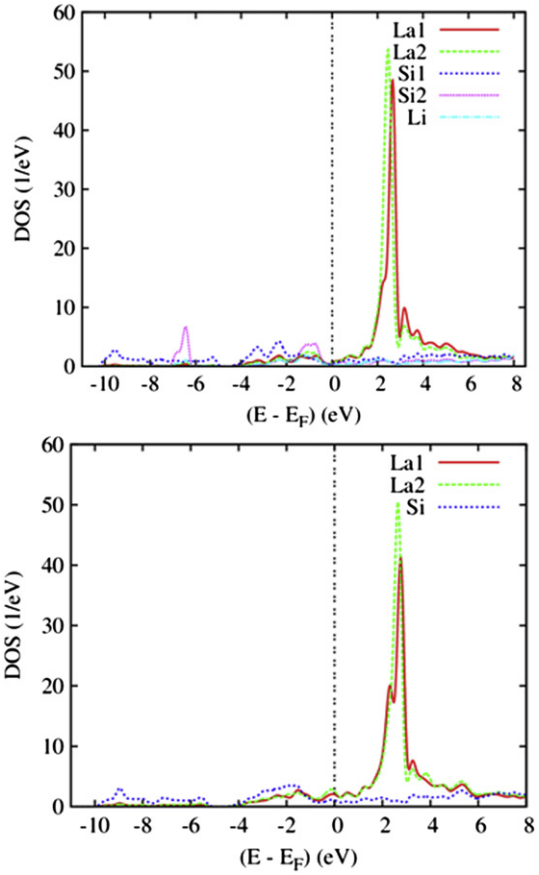

Fig. 5. Site projected density of states for $La_2Li_2Si_3$ (top) and LaSi (bottom).

present for the three types of interactions: La1–Si(Si1), La2–Si(Si1) and Si–Si (Si1–Si1). The slightly negative *i*COOP intensities in the lower part of the VB are due to the involvement of Si states in the Si–Si bonding; they are, however more antibonding in LaSi because some La1/La1 interact only with Si while some bonding is also found between Li and La as shown in the upper panel. Otherwise the whole VB is of bonding character in both compounds. The interactions proper to the ternary silicide (top panel) include the Si2 substructure. They exhibit less La1–Si2 bonding, while La2–Si2 interaction has similar intensity to La1–Si1. This likely arises from the short La2–Si2 = 319 pm distance and the location of the Si2 atoms within Li_4La_2 prisms. Also it is relevant to note the negligible Si2–Si2 bonding in agreement with the crystal chemical description of *isolated* Si2 with no Si–Si bonding. Turning to the Li interactions with the La and Si substructures, Fig. 7 shows the different bonding with most intense *i*COOP for Li–Si2 which results from the coordination of Li with two Si2 at 266.9 pm and 1 Si2 at 277.6 pm, while less intense Li–Si1 *i*COOP result from the neighbouring with one Si1 at 262.9 pm. Li–La bonding is only significant for La2 with two La2 at 315.4 pm and one La2 at 315.9 pm, while negligibly small Li–La1 are observed.

The emerging picture of the chemical bonding within $La_2Li_2Si_3$ is reminiscent of that in binary LaSi together with new features brought by the insertion of the Li and Si2 substructures.

3.4. ^{7}Li and ^{29}Si solid state NMR

Figs. 8 and 9 show the ^{7}Li and ^{29}Si MAS-NMR spectra at room temperature. Only a single resonance at 8 ppm versus 1 M aqueous LiCl solution is observed, in agreement with the presence of only a single site in the crystal structure. The resonance shift of this signal suggests the presence of a small amount of residual valence electron density on the lithium atom, suggesting incomplete ionization in a slight deviation from the Zintl concept. More significant deviations are observed for the two silicon species. Two signals are observed (near 800 and 273 ppm versus tetramethylsilane), whose integrated peak area ratio is 28:72 in reasonable agreement with the crystal structure prediction (33:67). While the Larmor frequency of the Si1 species might still be considered to be predominantly caused by a chemical shift effect arising from bond covalence effects in these Si–Si bonded chain units, the strongly

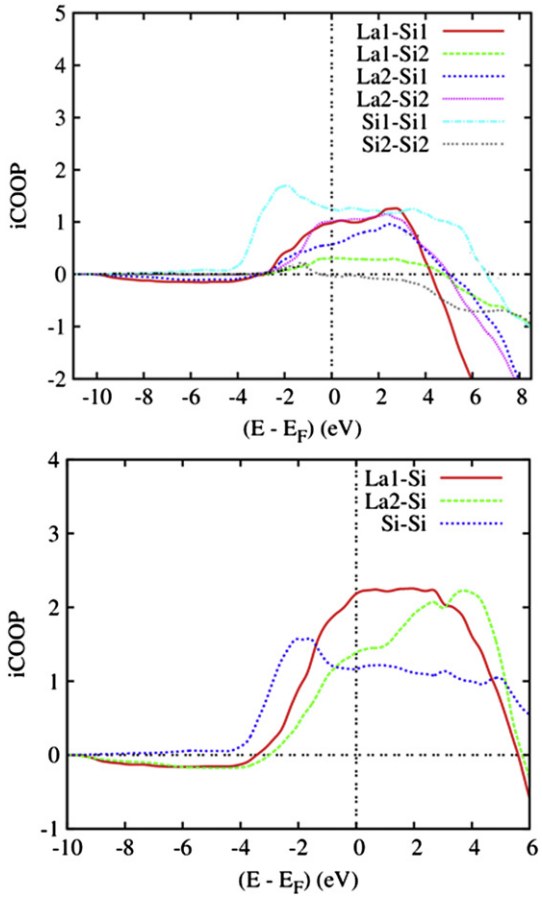

Fig. 6. Chemical bonding based on integrated COOP (*i*COOP) for $La_2Li_2Si_3$ (top) and LaSi (bottom).

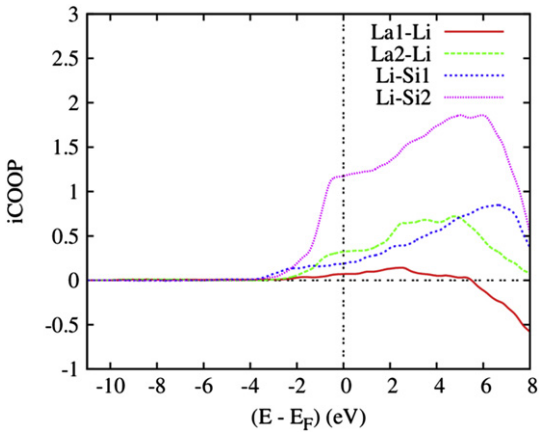

Fig. 7. Chemical bonding based on integrated COOP (*i*COOP) for Li interactions with the La and Si substructures in $La_2Li_2Si_3$.

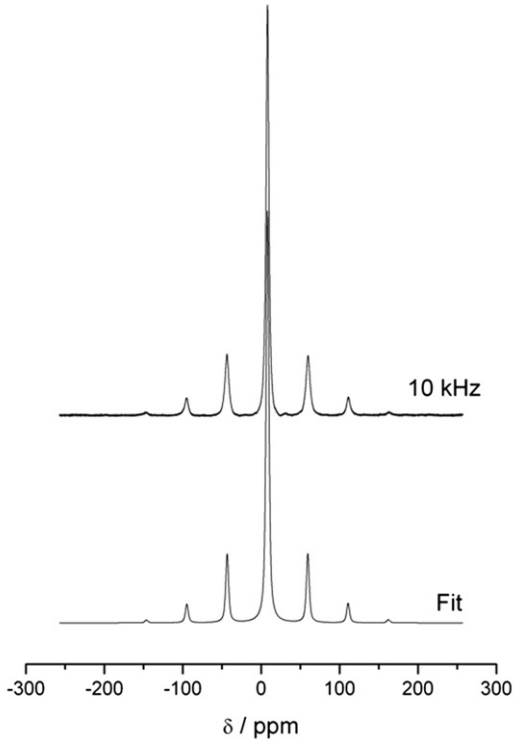

Fig. 8. ^{7}Li MAS-NMR spectrum for $Li_2La_2Si_3$ at a spinning frequency of 10 kHz. Top: experimental spectrum. Bottom: simulated spectrum based on a nuclear quadrupolar coupling constant of 49 kHz. Minor peaks are spinning sidebands arising from the non-central Zeeman transitions.

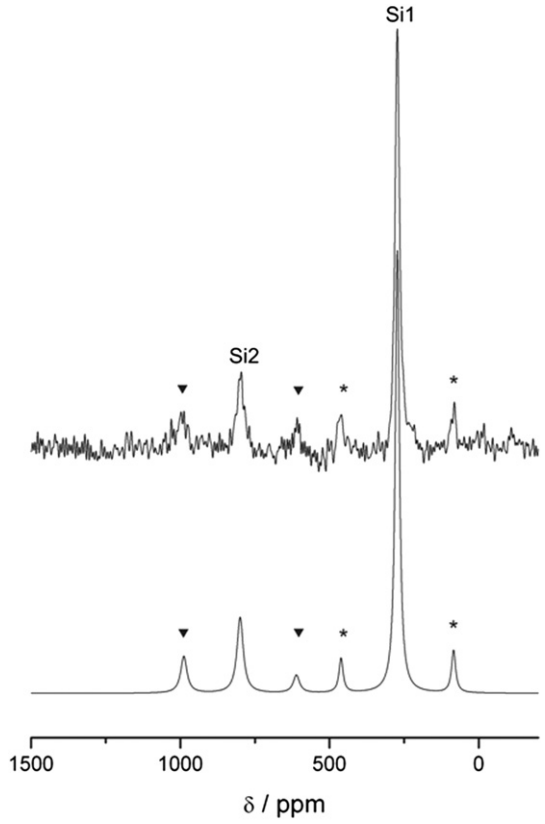

Fig. 9. ^{29}Si MAS-NMR spectrum of $La_2Li_2Si_3$. Top: experimental data, bottom: simulations. Spinning sidebands originating from chemical shift anisotropy effects are indicated by asterisks for Si1 and by triangles for Si2.

high-frequency shifted resonance for the isolated Si2 atom suggests a Knight shift effect arising from substantial unpaired conduction electron spin density at the silicon nuclei (consistent with the Si2 contribution to the total DOS at higher energy). Nevertheless, the shift of the Si1 species is comparable to that observed in binary lithium silicides [8], which are well known to disobey the electron counting rules of Zintl, Klemm and Busmann [9] and show an incomplete electron transfer of 0.73 electrons per lithium on an average according to DFT calculations [48]. In addition, the spinning sideband intensities associated with this signal indicate a significant magnetic shielding anisotropy. Thus, the bonding state of this silicon atom differs substantially from that of a Si^{4-} species, consistent with the results from the Bader charge analysis. Fig. 10 summarizes the results from temperature dependent static ^{7}Li NMR experiments. All the three Zeeman transitions are observed, the outer ones of which are broadened by the anisotropy of first-order quadrupolar perturbations. From lineshape simulations using the DMFIT program, the quadrupolar coupling constant can be estimated as 49 kHz. Concerning the central $1/2 \leftrightarrow -1/2$ transition, no motional narrowing between 300 and 400 K is observed, indicating the absence of lithium ion dynamics on the kHz timescale within this temperature range.

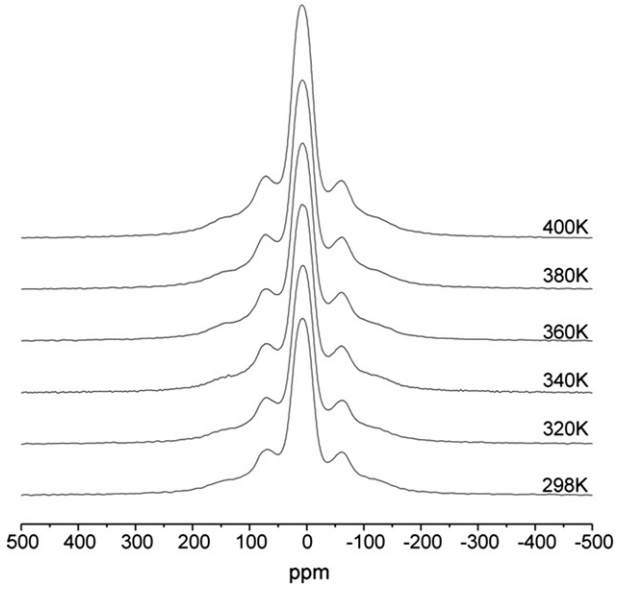

Fig. 10. Static ^{7}Li NMR spectra of $La_2Li_2Si_3$ as a function of temperature.

Acknowledgements

We thank Dipl.-Ing. U. Ch. Rodewald for the intensity data collection. This work was financially supported by the Deutsche Forschungsgemeinschaft (PAK 177) and the Bundesministerium für Forschung und Technologie (LiVe – Lithium-Verbundstrukturen within the programme LIB 2015). S.D. acknowledges a personal fellowship from the Fond der Chemischen Industrie.

References

[1] U. Kasavajjula, C. Wang, A. John Appleby, J. Power Sources 163 (2007) 1003.
[2] M.N. Obrovac, L.J. Krause, J. Electrochem. Soc. 154 (2007) A103.
[3] V.L. Chevrier, J.R. Dahn, J. Electrochem. Soc. 157 (2010) A392.
[4] B. Key, R. Bhattacharyya, M. Morcrette, V. Seznéc, J.-M. Tarascon, C.P. Grey, J. Am. Chem. Soc. 131 (2009) 9239.
[5] B. Key, M. Morcrette, J.-M. Tarascon, C.P. Grey, J. Am. Chem. Soc. 133 (2011) 503.
[6] A. Kuhn, P. Sreeraj, R. Pöttgen, H.-D. Wiemhöfer, M. Wilkening, P. Heitjans, J. Am. Chem. Soc. 133 (2011) 11018.
[7] A. Kuhn, P. Sreeraj, R. Pöttgen, H.-D. Wiemhöfer, M. Wilkening, P. Heitjans, Angew. Chem. 123 (2011) 12305.
[8] S. Dupke, T. Langer, R. Pöttgen, M. Winter, H. Eckert, Solid State NMR 40 (in press). http://dx.doi.org/10.1016/j.ssnmr.2011.09.002.
[9] R. Nesper, Prog. Solid State Chem. 20 (1990) 1.
[10] T. Dinges, U. Ch. Rodewald, S.F. Matar, H. Eckert, R. Pöttgen, Z. Anorg. Allg. Chem. 635 (2009) 1894.
[11] R. Pöttgen, T. Dinges, H. Eckert, P. Sreeraj, H.-D. Wiemhöfer, Z. Phys. Chem. 224 (2010) 1475.
[12] V.V. Pavlyuk, V.K. Pecharskii, O.I. Bodak, Dopov. Akad. Nauk. Ukr. RSR, Ser. B 2 (1989) 50.
[13] V.V. Pavlyuk, O.I. Bodak, Russ. Metall. 2 (1993) 181.
[14] Q. Xie, R. Nesper, Z. Anorg. Allg. Chem. 632 (2006) 1743.
[15] A. Czybulka, G. Steinberg, H.-U. Schuster, Z. Naturforsch 34b (1979) 1057.
[16] G. Steinberg, H.-U. Schuster, Z. Naturforsch 34b (1979) 1237.
[17] V.V. Pavlyuk, V.K. Pecharskii, O.I. Bodak, V.A. Bruskov, Soc. Phys. Crystallogr. 33 (1988) 24 Kristallografiya 33 (1988) 46.
[18] F. Merlo, A. Palenzona, M. Pani, S.K. Dhar, R. Kulkarni, J. Alloys Compd 394 (2005) 101.
[19] R. Pöttgen, Th. Gulden, A. Simon, GIT Labor-Fachzeitschrift 43 (1999) 133.
[20] R. Pöttgen, A. Lang, R.-D. Hoffmann, B. Künnen, G. Kotzyba, R. Müllmann, B.D. Mosel, C. Rosenhahn, Z. Kristallogr 214 (1999) 143.
[21] K. Yvon, W. Jeitschko, E. Parthé, J. Appl, Crystallogr 10 (1977) 73.
[22] G.M. Sheldrick, SHELXL-97, Program for Crystal Structure Refinement, University of Göttingen, Germany, 1997.
[23] G.M. Sheldrick, Acta Crystallogr. A64 (2008) 112.
[24] P. Hohenberg, W. Kohn, Phys. Rev. 136 (1964) B864.
[25] W. Kohn, L.J. Sham, Phys. Rev. 140 (1965) A1133.
[26] G. Kresse, J. Furthmüller, Phys. Rev. B 54 (1996) 11169.
[27] G. Kresse, J. Joubert, Phys. Rev. B 59 (1999) 1758.
[28] P.E. Blöchl, Phys. Rev. B 50 (1994) 17953.
[29] J. Perdew, K. Burke, M. Ernzerhof, Phys. Rev. Lett. 77 (1996) 3865.
[30] W.H. Press, B.P. Flannery, S.A. Teukolsky, W.T. Vetterling, Numerical Recipes, Cambridge University Press, New York, 1986.
[31] M. Methfessel, A.T. Paxton, Phys. Rev. B 40 (1989) 3616.
[32] H.J. Monkhorst, J.D. Pack, Phys. Rev. B 13 (1976) 5188.
[33] A.R. Williams, J. Kübler, C.D. Gelatt, Phys. Rev. B 19 (1979) 6094.
[34] V. Eyert, The Augmented Spherical Wave Method – A Comprehensive Treatment, Lecture Notes in Physics, Springer, Heidelberg, 2007.

[35] R. Hoffmann, Angew. Chem. Int. Ed. Engl. 26 (1987) 846.
[36] D. Massiot, F. Fayon, M. Capron, I. King, S. Le Calvé, B. Alonso, J.O. Durand, B. Bujoli, Z. Gan, G. Hoatson, Magn. Reson. Chem. 40 (2002) 70.
[37] Q.-X. Xie, R. Nesper, Z. Kristallogr. NCS 218 (2003) 289.
[38] Q.-X. Xie, R. Nesper, Z. Kristallogr. NCS 219 (2004) 83.
[39] I. Todorov, S.C. Sevov, Inorg. Chem. 44 (2005) 5361.
[40] E. Parthé, B. Chabot, Crystal structures and crystal chemistry of ternary rare earth-transition metal borides, silicides and homologues, in: K.A. GschneidnerJr., L. Eyring (Eds.), Handbook on the Physics and Chemistry of Rare Earths, Vol. 6, Elsevier, Amsterdam, 1984, pp. 113–334 (Chapter 48).
[41] E. Parthé, L. Gelato, B. Chabot, M. Penzo, K. Cenzual, R. Gladyshevskii, TYPIX–Standardized Data and Crystal Chemical Characterization of Inorganic Structure Types. Gmelin Handbook of Inorganic and Organometallic Chemistry, eighth ed. Springer, Berlin, 1993.
[42] Hj Mattausch, O. Oeckler, A. Simon, Z. Anorg. Allg. Chem. 625 (1999) 1151.
[43] J. Donohue, The Structures of the Elements, Wiley, New York, 1974.
[44] R.-D. Hoffmann, Zh. Wu, R. Pöttgen, Eur. J. Inorg. Chem. (2003) 3425.
[45] T. Dinges, R.-D. Hoffmann, L. van Wüllen, P. Henry, H. Eckert, R. Pöttgen, J. Solid State Electrochem. 15 (2011) 237.
[46] J. Emsley, The Elements, Clarendon Press, Oxford, 1989.
[47] R. Nesper, H.G. von Schnering, J. Curda, Chem. Ber. 119 (1986) 3576.
[48] V.L. Chevrier, J.W. Zwanziger, J.R. Dahn, J. Alloys Compd 496 (2010) 25.
[49] A.D. Becke, K.E. Edgecombe, J. Chem. Phys. 92 (1990) 5397.
[50] R. Bader, Chem. Rev. 91 (1991) 893.